RSC Advances

PAPER

View Article Online
View Journal | View Issue

Cite this: *RSC Adv.*, 2022, **12**, 26808

Lattice dynamic stability and electronic structures of ternary hydrides $La_{1-x}Y_xH_3$ *via* first-principles cluster expansion

Prutthipong Tsuppayakorn-aek, [ab] Wiwittawin Sukmas,[ab] Prayoonsak Pluengphon, [c] Burapat Inceesungvorn, [d] Piya Phansuke,*[e] Pungtip Kaewtubtim,[e] Rajeev Ahuja, [fg] Thiti Bovornratanaraks *[ab] and Wei Luo [f]

Received 20th May 2022
Accepted 8th August 2022

DOI: 10.1039/d2ra03194a

rsc.li/rsc-advances

Lanthanum hydride compounds LaH_3 become stabilized by yttrium substitution under the influence of moderate pressure. Novel materials with a wide range of changes in the structural properties as a function of hydrogen are investigated by means of the first-principles cluster expansion technique. Herein, the new compounds $La_{1-x}Y_xH_3$, where $0 \leq x \leq 1$, are determined to adopt tetragonal structures under high-pressure with the compositions $La_{0.8}Y_{0.2}H_3$, $La_{0.75}Y_{0.25}H_3$, and $La_{0.5}Y_{0.5}H_3$. The corresponding thermodynamic and dynamical stabilities of the predicted phases are confirmed by a series of calculations including, for example, phonon dispersion, electronic band structure, and other electronic characteristics. According to the band characteristics, all hydrides except that of $I4_1/amd$ symmetry are semiconductors. The tetragonal $La_{0.5}Y_{0.5}H_3$ phase is found to become semi-metallic, as confirmed by adopting the modified Becke–Johnson exchange potential. The physical origins of the semiconductor properties in these stable hydrides are discussed in detail. Our findings provide a deeper insight into this class of rare-earth ternary hydrides.

1 Introduction

Hydrogen-rich materials have attracted considerable attention thanks to their potential applications, especially in hydrogen storage,[1–3] as well as the changes in physical and chemical properties as a function of the hydrogen concentration.[4–8] The electronic structures of several rare-earth hydrides have been widely investigated,[9–17] for example, the metal–semiconductor transition in lanthanum dihydride and lanthanum trihydride.[9] Also, lanthanum deuterium was observed by neutron diffraction measurements[18] to form NaCl-type LaD at high pressures as a result of pressure-induced decomposition of $LaH_{2.3}$ *via* dismutation. This phase separation[19] is due to the influence of H atoms moving into the empty O-sites of the surrounding $LaH_{2.3}$. Following this, by means of first-principles calculations, LaH was predicted to become thermodynamically and dynamically stable at a pressure of 15 GPa. The pressure-dependent disproportionation reaction of LaH_2 was also observed by high-pressure infrared reflection and Raman scattering measurements. Reportedly, at frequency ranging from 14 to 30 GPa, the absorption peaks found are similar to those observed in LaH_3.[20]

In recent years, both experimental and theoretical studies of rare-earth trihydrides have been reported. Face-centered cubic ScH_3, YH_3, and LaH_3 rare-earth trihydrides were predicted to be dynamically stable and become superconducting at high pressures.[21,22] The fcc YH_3 superconducts at a relatively high superconducting transition temperature (T_c) close to 40 K at 18 GPa.[21] According to the aforementioned experimental findings[9] and recent extensive studies by first-principles calculations,[23,24] LaH_3 was demonstrated to have an energy gap of 0.8–0.9 eV. Moreover, the LaH_3 and YH_3 compounds were confirmed theoretically to be structurally stable at 11 GPa and 18 GPa, respectively.[21,22] At this stage, alloying these mentioned rare-earth elements, by means of the cluster expansion (CE) technique, might give rise to new hydrides with novel physical properties. To thoroughly investigate electronic properties in the candidate structure of $La_{1-x}Y_xH_3$, calculations should be

[a]*Extreme Conditions Physics Research Laboratory and Center of Excellence in Physics of Energy Materials (CE:PEM), Department of Physics, Faculty of Science, Chulalongkorn University, Bangkok 10330, Thailand. E-mail: thiti.b@chula.ac.th*
[b]*Thailand Center of Excellence in Physics, Ministry of Higher Education, Science, Research and Innovation, 328 Si Ayutthaya Road, Bangkok 10400, Thailand*
[c]*Division of Physical Science, Faculty of Science and Technology, Huachiew Chalermprakiet University, Samutprakarn 10540, Thailand*
[d]*Department of Chemistry, Center of Excellence in Materials Science and Technology and Materials Science Research Centre, Faculty of Science, Chiang Mai University, Chiang Mai, 50200, Thailand*
[e]*Department of Science, Faculty of Science and Technology, Prince of Songkla University, Pattani, 94000, Thailand. E-mail: piya.p@psu.ac.th*
[f]*Materials Theory, Department of Physics and Materials Science, Uppsala University, Box 530, SE-751 21, Uppsala, Sweden*
[g]*Department of Physics, Indian Institute of Technology (IIT) Ropar, Rupnagar 140001, Punjab, India*

conducted at moderate pressures, as consistent with the reports on LaH_3 being thermodynamically stable up to at least 20 GPa.[18] As a consequence, first-principles CE will be performed at 20 GPa for the new class of $La_{1-x}Y_xH_3$ substituted rare-earth hydrides. In this regard, we attempt to (i) search for stable compositions and favored atomic configurations of $La_{1-x}Y_xH_3$, (ii) to look for signs of superconducting properties in these stable compositions, and (iii) to better understand any changes in the materials' properties induced by the substitution of the Y atom.

Herein, we make use of the first-principles CE based on density functional theory as a starting point to first define the stable $La_{1-x}Y_xH_3$ alloy(s). CE is conducted at 20 GPa due to the possible chemical reaction between LaH_3 and YH_3 solid solution achievable at 15 GPa and 18 GPa, respectively.[18,21] Then the concentration x is varied from 0 to 1, while the GS structures of the La–Y–H system as well as their formation energies are determined correspondingly. Based on the density functional theory (DFT), CE calculations output ground-state candidate structures along the convex hull.[3,25,26] Note that the CE calculation is associated with a set of lattice sites appointed as an occupation variable in a crystal structure. Clearly, an occupation variable in a given crystal structure leads to a decrease in the crystal symmetry. In our case, the role of the Y atom induces the decrease in symmetry of fcc-LaH_3, which is expected to exhibit structural phase transitions under pressure. The resulting semiconducting properties of the La–Y–H systems are then compared and discussed.

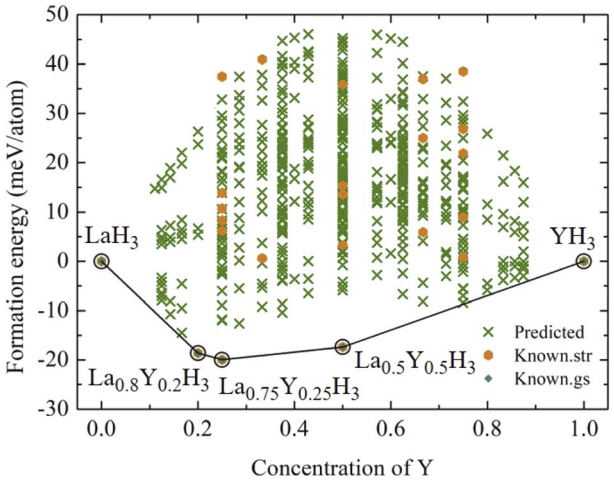

Fig. 1 The formation energy at 20 GPa is shown by a convex hull. The predicted structures refer to structures whose energies have not yet been calculated from DFT, the known str refers to structures whose energies have been calculated from DFT, and the known gs refers to ground state energies that have so far been confirmed by DFT.

2 Computational details

A substitution of an atomic type can be determined by the cluster expansion (CE) method,[27] while the energy of which is reported as a function of substituted occupation. This is done by using the MIT Ab initio Phase Stability (MAPS) code,[28] as implemented in the Alloy-Theoretic Automated Toolkit (ATAT).[29] These codes are available in the Quantum Espresso (QE) package.[30] The technical details of the CE calculations have been described extensively in ref. 3, 26, 31 and 32. The plane-wave energy cutoff of 60 Ry and k-point meshes of 4000 were used. The generalized gradient approximation proposed by Perdew, Burke, and Ernzerhof (GGA-PBE)[33] was used as the exchange–correlation functional. All structures were calculated by imposing lattice dynamics, by means of a supercell approach, as implemented in Cambridge Serial Total Energy Package (CASTEP) code.[34] As for the band structure evaluation, the modified Becke–Johnson (mBJ) exchange potential[35] in conjunction with the GGA functional were used to determine the energy gap, as implemented in the Vienna ab initio simulation package (VASP) code.[36] The nature of chemical bonding was further demonstrated by evaluating the electron localization function (ELF),[37] as also implemented in VASP code, together with the projected crystal orbital overlap

Table 1 The optimized structural parameters of the La–Y–H system obtained from the first-principles calculations

Space group	Pressure (GPa)	Lattice parameters (Å, °)	Atomic coordinates (fractional)
$I4/m$	20	$a = 8.096$ $b = 8.096$ $c = 4.992$ $\alpha = 90$ $\beta = 90$ $\gamma = 90$	Y1 (0, 0, 0) La1 (0.203, 0.6018, 0) H1 (0.1909, 0.092, 0.5) H2 (0.388, 0.192, 0.50) H3 (0, 0.5, 0.25) H4 (0, 0, 0.25)
$I4/mmm$	20	$a = 5.073$ $b = 5.073$ $c = 10.723$ $\alpha = 90$ $\beta = 90$ $\gamma = 90$	Y1 (0, 0, 0) La1 (0.5, 0, 0.25) La2 (0, 0, 0.5) H1 (0, 0, 0.730) H2 (0.265, 0.265, 0.620) H3 (0.5 0, 0)
$I4_1/amd$	20	$a = 5.078$ $b = 5.078$ $c = 10.749$ $\alpha = 90$ $\beta = 90$ $\gamma = 90$	Y1 (0.5, 0.5, −0.5) La1 (0, 0.5, −0.25) H1 (0.5, 0.5, −0.233) H2 (0.25, 0.726, −0.625)

population (pCOOPs),[38] which is implemented in the LOBSTER code.[39]

3 Results and discussion

We explored the effect of Y substitution on the face-centered cubic LaH_3 at 20 GPa by means of the first-principles CE. Structures predicted from CE have yet to be confirmed by DFT. The stable compositions are determined in terms of minimum free energy along the function of atomic occupation, which is defined by eqn (1).

$$E(\sigma) = \sum_{\sigma} m_{\alpha} J_{\alpha} \left\langle \prod_{i \in \alpha'} \sigma_i \right\rangle, \quad (1)$$

where the total energy ($E(\sigma)$) is defined as a function of cluster (α) from which a set of lattice sites i can be represented. σ_i denotes an occupation variable or a configuration at lattice sites i. The coefficients J_{α}, called the effective cluster interactions, together with the multiplicities m_{α} being symmetrically equivalent to α, are evaluated based on the DFT-obtained structures ("Known.str"), to generate candidate structures which are referred to as "Predicted". Finally, the ground state structures are the ones with relatively lowest energies along the convex hull.

According to Fig. 1, the most relatively stable structures along the convex hull are those of $La_{0.8}Y_{0.2}H_3$, $La_{0.75}Y_{0.25}H_3$, and $La_{0.5}Y_{0.5}H_3$. These candidate alloys undergo a structural relaxation calculated based on DFT under the pressure of 20 GPa. The optimized structural parameters of which are reported in Table 1. Markedly, substituting Y into the fcc-LaH_3 significantly affects its structural behaviour, that is, the fcc structure with space group of $Fm\bar{3}m$ successively transitions from high- to low-symmetry structures (*i.e.* $Fm\bar{3}m \rightarrow I4/m$, $Fm\bar{3}m \rightarrow I4/mmm$, and $Fm\bar{3}m \rightarrow I4_1/amd$), as can be seen in Fig. 2. Note that for all our calculations regarding the $La_{1-x}Y_xH_3$ alloys, all the corresponding structures are evaluated without taking into consideration the entropy (S) contributions due to the fact that DFT works at 0 K and is capable of determining compounds closely resembling those found in experiment.[40–46]

At this stage, it is worth mentioning once again that at the pressure of 20 GPa, $La_{0.8}Y_{0.2}H_3$, $La_{0.75}Y_{0.25}H_3$, and $La_{0.5}Y_{0.5}H_3$ have negative energies of formation relative to those of LaH_3 and YH_3. Although formation energy suggests thermodynamic stability, it does not suffice to guarantee the existence of such compounds. Thus, it is of utmost importance to also conduct phonon calculations to ensure dynamical stability for the candidate compounds. Fig. 3 reports the phonon dispersions at 20 GPa of $La_{0.8}Y_{0.2}H_3$ (a), $La_{0.75}Y_{0.25}H_3$ (b), and $La_{0.5}Y_{0.5}H_3$ (c), which are clearly stable due to the absence of imaginary frequencies of any dispersion branches. As for the possibility of such compounds to form at varying temperatures, thermal effects on the dynamical stability must be taken into account in phonon calculations.[47]

Now, the electronic characteristics of the $I4/m$, $I4/mmm$, and $I4_1/amd$ La–Y–H systems are thoroughly investigated to look for

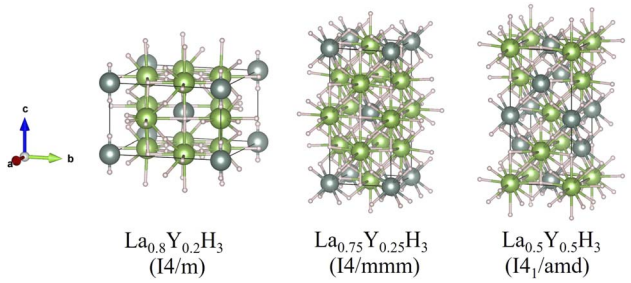

Fig. 2 Structures of the La–Y–H system. The pink, dark green, and light green spheres represent hydrogen, lanthanum, and yttrium atoms, respectively.

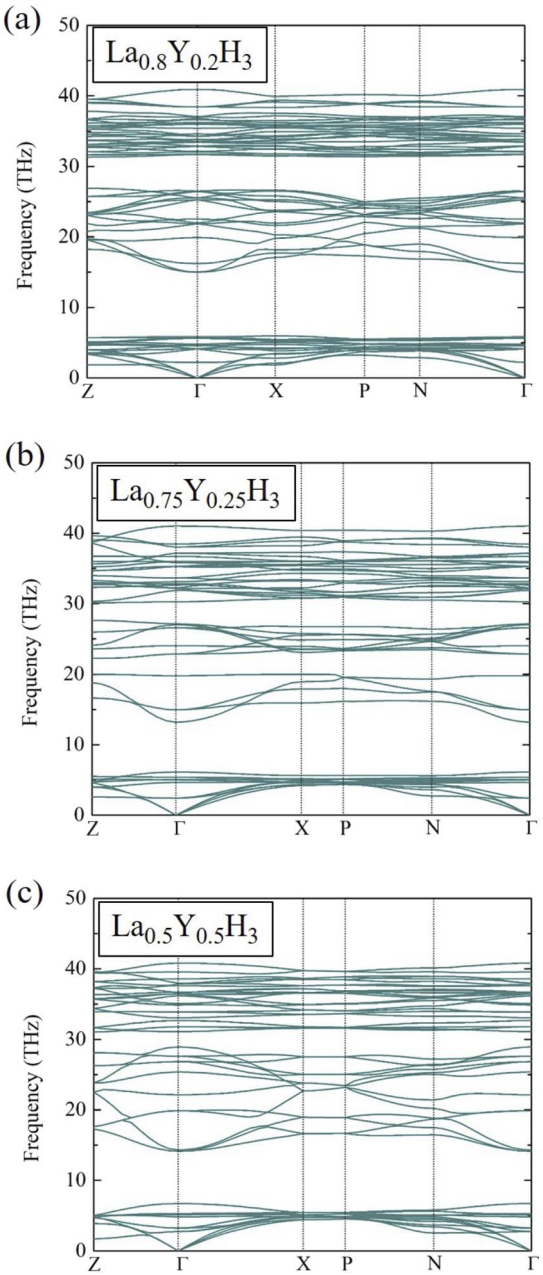

Fig. 3 Phonon dispersions of (a) $La_{0.8}Y_{0.2}H_3$ at 20 GPa, (b) $La_{0.75}Y_{0.25}H_3$ at 20 GPa, and (c) $La_{0.5}Y_{0.5}H_3$ at 20 GPa.

signs of possible superconductivity in these materials. The corresponding electronic band structures of these compounds are shown in Fig. 4, all of which are determined using the GGA-PBE exchange–correlation functional. As a result, the *I*4/*m*, *I*4/*mmm*, and $I4_1/amd$ structures become semiconductors with indirect band gaps of 0.765, 0.382, and 0.335 eV, respectively. Note that GGA underestimates band gaps in many semiconducting systems. Therefore, we additionally perform the calculation based on the hybrid exchange–correlation functional to correct the mentioned discrepancy. Despite being considered to be one of the most effective functionals capable of accurately determining band gaps, the Heyd–Scuseria–Ernzerhof (HSE06) functional is itself computationally expensive. Thus, we opt for the modified Becke–Johnson (mBJ) exchange potential[35] in conjunction with the GGA functional, owing to the fact that the former determines band gaps even of strongly correlated systems with an acceptable level of accuracy, yet with fewer resources compared to HSE06.[48–51] According to Fig. 4(b), the band dispersion of the *I*4/*m* structure, calculated by the mBJ exchange potential, clearly indicates a semiconducting phase with an indirect energy gap of 0.346 eV, whereas it is 0.252 eV in the case of the *I*4/*mmm* structure (Fig. 4(d)). Markedly, the $I4_1/amd$ La–Y–H (Fig. 4(g)) turns out to be semimetallic due to the presence of states across the Fermi level (E_F). A plausible explanation of which might be attributable to the strongly correlated nature of electrons in Y atoms when substituted into

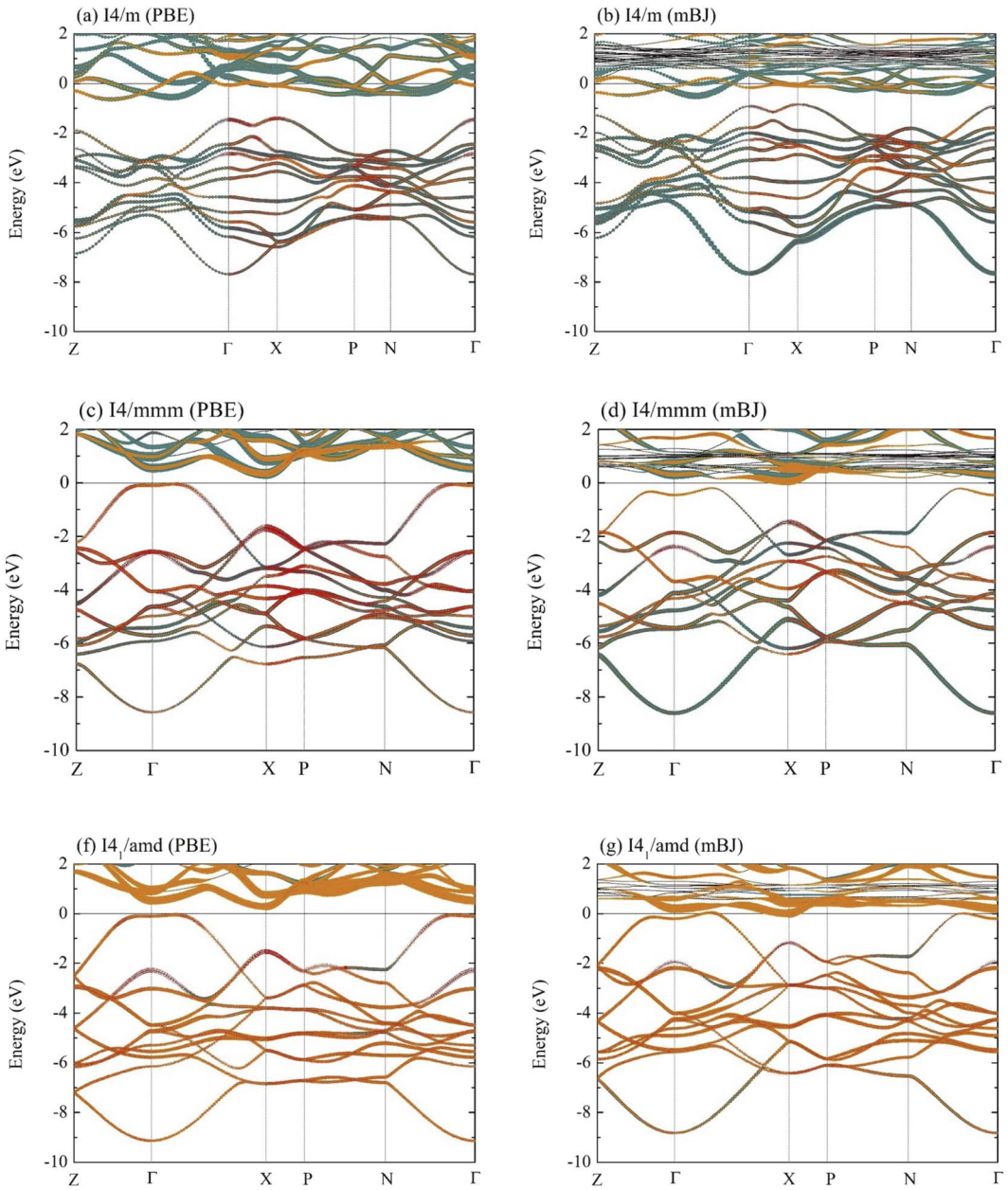

Fig. 4 Band structures calculated by the GGE-PBE of (a) the *I*4/*m* structure at 20 GPa, (c) the *I*4/*mmm* structure at 20 GPa, and (f) the $I4_1/amd$ structure at 20 GPa. Band structures calculated by incorporating the mBJ exchange potential of (b) the *I*4/*m* structure at 20 GPa, (d) the *I*4/*mmm* structure at 20 GPa, and (g) the $I4_1/amd$ structure at 20 GPa. The dark cyan, orange, and red colors represent, respectively, La, Y, and H atoms.

the compound, as highlighted by the increased size of dispersion branches above E_F (Fig. 4(g)).

Also we further analyze the electronic structures by means of the charge density differences of the *I*4/*m*, *I*4/*mmm*, and *I*4$_1$/*amd* structures, which are illustrated in Fig. 5. The charge density difference in the La–Y–H systems is expressed as,

$$\rho_{net} = \rho_{La_{1-x}Y_xH_3} - \rho_Y - \rho_H, \quad (2)$$

where $\rho_{La_{1-x}Y_xH_3}$ denotes the calculated charge of $La_{1-x}Y_xH_3$, while ρ_Y and ρ_H represent the charge densities of the isolated Y and H atoms, respectively. The charge density illustrates the stronger interaction between Y and its neighboring atoms, *i.e.* La and H.

Another aspect that needs to be considered is the nature of chemical bonding, which can be observed in theory *via* the electron localization function (ELF)[37] and the projected crystal orbital overlap population (pCOOPs), both of which play a crucial role in describing the electron accumulation and determining anti-bonding and bonding characteristics.[52] As a consequence, the calculations of ELF for all the *I*4/*m*, *I*4/*mmm*, and *I*4$_1$/*amd* ternary hydrides are made and reported in Fig. 6. In the case of *I*4/*m* (Fig. 6(a)), it is noticeable that electrons tend to accumulate around H atoms which also display some electronic distribution in the vicinity of both La and Y atoms, indicating the possibility of weak bonding between the first nearest-

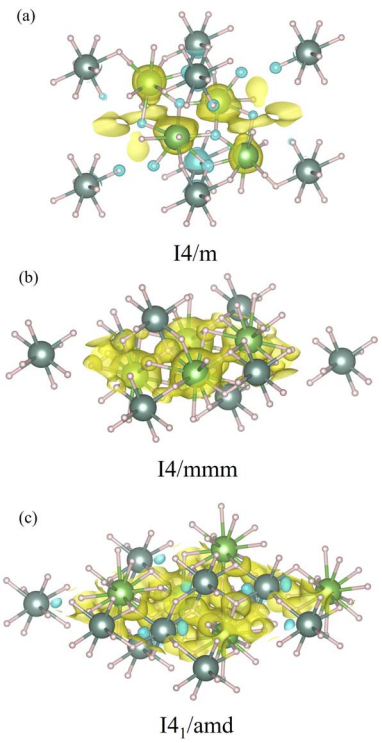

Fig. 5 The charge density differences of (a) the *I*4/*m* structure, (b) the *I*4/*mmm* structure, and (c) the *I*4$_1$/*amd* structure. The yellow and cyan colors represent the charge accumulation and depletion regions, respectively. The iso-values of (a) the *I*4/*m* structure, (b) the *I*4/*mmm* structure, and (c) the *I*4$_1$/*amd* structure are set to be 0.04 e Å, 0.02 e Å, and 0.02 e Å, respectively.

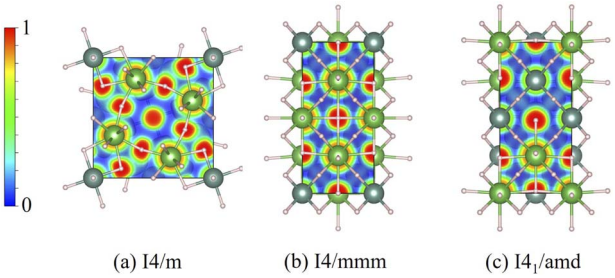

Fig. 6 The localization function (ELF) of (a) the *I*4/*m* structure at 20 GPa, as plotted in the (001) plane, (b) the *I*4/*mmm* structure at 20 GPa, as plotted in the (010) plane, and (c) the *I*4$_1$/*amd* structure at 20 GPa, as plotted in the (010) plane.

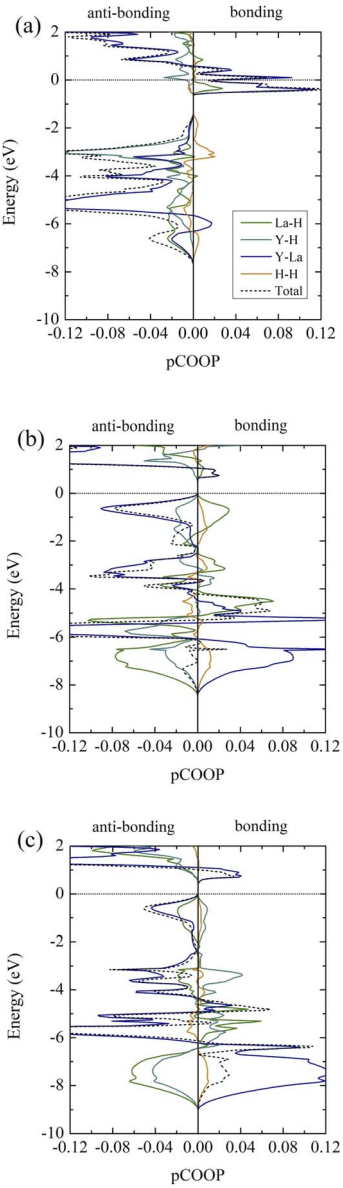

Fig. 7 Projected crystal orbital overlap populations (pCOOPs) of (a) the *I*4/*m* structure at 20 GPa, (b) the *I*4/*mmm* structure at 20 GPa, and (c) the *I*4$_1$/*amd* structure at 20 GPa, respectively.

neighbor (NN) La–H (2.2584 Å) and the second NN Y–H (2.0980 Å). On the other hand, electrons tend to localize around each metal in the cases of $I4/mmm$ and $I4_1/amd$, as can be seen in the Fig. 6(b) and (c).

It is clear that, according to the ELF in all cases, H atoms are unlikely to chemically bond with La and Y atoms. Thus, we further investigate the bond characteristics by performing the pCOOP calculations[53–56] for all materials in question. As a result, the pCOOP calculations for all La–Y–H hydrides are reported in Fig. 7. Shown in Fig. 7(a), $I4/m$ largely consists of anti-bonding between La–H pairs at energies ranging from −0.65 eV to −0.05 eV, while the La–Y pairs dominate at energies ranging from −0.65 eV and all the way up to E_F. A lesser contribution from the Y–H pairs and the H–H pairs can be found from −0.64 eV to the Fermi level and −0.54 eV to −0.05 eV, respectively, both of which are anti-bonding states. As for the $I4/mmm$ structure, the La–Y pairs displayed a higher degree of the anti-bonding states starting from −2.20 eV to the Fermi level and so do the Y–H pairs. On the contrary, the La–H and the H–H pairs characterized by ionic states are noticeable from −2.25 eV to −0.05 eV and −2.15 eV to −0.05 eV, respectively (Fig. 7(b)). Lastly, a larger amount of the anti-bonding states attributed from the La–Y pairs dwell at energies ranging from −2.34 eV to the Fermi level. Similar bond characteristics are observable for those of La–H and La–Y pairs, whereas the Y–H and H–H pairs tend to have a lesser degree of ionic states from 2.34 eV to −0.1 eV, as can be seen in Fig. 7(c).

4 Conclusion

In summary, we report novel rare-earth substituted $La_{1-x}Y_xH_3$ alloys under the influence of moderate pressure by adopting the first-principles cluster expansion technique. The relatively lowest energy structures along the convex hull are $La_{0.8}Y_{0.2}H_3$, $La_{0.75}Y_{0.25}H_3$, and $La_{0.5}Y_{0.5}H_3$, all of which are confirmed dynamically stable at 20 GPa. By adopting the modified Becke–Johnson (mBJ) exchange potential, band characteristics of such materials are determined. Also, charge density difference, localization function, and projected crystal orbital overlap population are evaluated to further investigate the corresponding electronic behaviors. However, the stable structures of $La_{0.8}Y_{0.2}H_3$, $La_{0.75}Y_{0.25}H_3$, and $La_{0.5}Y_{0.5}H_3$ have yet to be observed experimentally. We believe that our findings will urge further first-principles calculations as well as experiments for the exploration of this class of rare-earth substituted hydride superconductors.

Conflicts of interest

There are no conflicts to declare.

Acknowledgements

This research project is supported by the Second Century Fund (C2F), Chulalongkorn University. We gratefully acknowledge computational resources from the Swedish National Infrastructure for Computing, SNIC (2021/1-42). R. A. and W. L. acknowledge the support from the Swedish Research Council (Grant no. VR-2020-04410) and Gust. Richert stiftelse, Sweden (2021-00665). This project is funded by National Research Council of Thailand (NRCT): (NRCT5-RSA63001-04). This work is partially supported by the Center of Excellence in Materials Science and Technology, Chiang Mai University.

Notes and references

1 P. Pluengphon, T. Bovornratanaraks, P. Tsuppayakorn-aek, U. Pinsook and B. Inceesungvorn, *Int. J. Hydrogen Energy*, 2019, **44**, 21948–21954.
2 P. Pluengphon, P. Tsuppayakorn-aek, B. Inceesungvorn and T. Bovornratanaraks, *Int. J. Hydrogen Energy*, 2020, **45**, 25065–25074.
3 P. Pluengphon, P. Tsuppayakorn-aek, B. Inceesungvorn, R. Ahuja and T. Bovornratanaraks, *J. Phys. Chem. C*, 2021, **125**, 1723–1730.
4 J. L. Braun, S. W. King, E. R. Hoglund, M. A. Gharacheh, E. A. Scott, A. Giri, J. A. Tomko, J. T. Gaskins, A. Alkukhun, G. Bhattarai, M. M. Paquette, G. Chollon, B. Willey, G. A. Antonelli, D. W. Gidley, J. Hwang, J. M. Howe and P. E. Hopkins, *Phys. Rev. Mater.*, 2021, **5**, 035604.
5 M. Nordio, S. A. Wassie, M. V. S. Annaland, D. A. P. Tanaka, J. L. V. Sole and F. Gallucci, *Int. J. Hydrogen Energy*, 2021, **46**, 23417–23435.
6 A. Drexler, C. Bergmann, G. Manke, V. Kokotin, K. Mraczek, S. Leitner, M. Pohl and W. Ecker, *J. Alloys Compd.*, 2021, **856**, 158226.
7 Q. Cheng, C. Hu, G. Wang, Z. Zou, H. Yang and L. Dai, *J. Am. Chem. Soc.*, 2020, **142**, 5594–5601.
8 S. Jiang, R. Zhang, H. Liu, Y. Rao, Y. Yu, S. Chen, Q. Yue, Y. Zhang and Y. Kang, *J. Am. Chem. Soc.*, 2020, **142**, 6461–6466.
9 D. K. Misemer and B. N. Harmon, *Phys. Rev. B: Condens. Matter Mater. Phys.*, 1982, **26**, 5634–5644.
10 Y. Yao and D. D. Klug, *Phys. Rev. B: Condens. Matter Mater. Phys.*, 2010, **81**, 140104.
11 H. Liu, I. I. Naumov, R. Hoffmann, N. W. Ashcroft and R. J. Hemley, *Proc. Natl. Acad. Sci. U. S. A.*, 2017, **114**, 6990–6995.
12 Z. M. Geballe, H. Liu, A. K. Mishra, M. Ahart, M. Somayazulu, Y. Meng, M. Baldini and R. J. Hemley, *Angew. Chem., Int. Ed.*, 2018, **57**, 688–692.
13 H. Liu, I. I. Naumov, Z. M. Geballe, M. Somayazulu, J. S. Tse and R. J. Hemley, *Phys. Rev. B*, 2018, **98**, 100102.
14 A. P. Drozdov, P. P. Kong, V. S. Minkov, S. P. Besedin, M. A. Kuzovnikov, S. Mozaffari, L. Balicas, F. F. Balakirev, D. E. Graf, V. B. Prakapenka, E. Greenberg, D. A. Knyazev, M. Tkacz and M. I. Eremets, *Nature*, 2019, **569**, 528–531.
15 T. Sakai, M. Sakai, T. Kobayashi, M. Yasutake, S. Akisato, R. Mikami, N. Suganuma, Y. Takahashi, Y. Nakajima, M. Tokuda, *et al.*, *Thin Solid Films*, 2019, **669**, 288–293.
16 R. Kataoka, T. Kimura, K. Sakaki, M. Nozaki, T. Kojima, K. Ikeda, T. Otomo, N. Takeichi and A. Kamegawa, *Inorg. Chem.*, 2019, **58**, 13102–13107.

17 P. Tsuppayakorn-aek, U. Pinsook, W. Luo, R. Ahuja and T. Bovornratanaraks, *Mater. Res. Express*, 2020, **7**, 086001.
18 A. Machida, M. Honda, T. Hattori, A. Sano-Furukawa, T. Watanuki, Y. Katayama, K. Aoki, K. Komatsu, H. Arima, H. Ohshita, K. Ikeda, K. Suzuya, T. Otomo, M. Tsubota, K. Doi, T. Ichikawa, Y. Kojima and D. Y. Kim, *Phys. Rev. Lett.*, 2012, **108**, 205501.
19 A. Machida, T. Watanuki, D. Kawana and K. Aoki, *Phys. Rev. B: Condens. Matter Mater. Phys.*, 2011, **83**, 054103.
20 Y. Sakurai, A. Machida and K. Aoki, *Solid State Commun.*, 2011, **151**, 815–817.
21 D. Y. Kim, R. H. Scheicher, H.-k. Mao, T. W. Kang and R. Ahuja, *Proc. Natl. Acad. Sci. U. S. A.*, 2010, **107**, 2793–2796.
22 A. P. Durajski and R. Szcześniak, *Supercond. Sci. Technol.*, 2014, **27**, 115012.
23 E. K. Chang, X. Blase and S. G. Louie, *Phys. Rev. B: Condens. Matter Mater. Phys.*, 2001, **64**, 155108.
24 J. A. Alford, M. Y. Chou, E. K. Chang and S. G. Louie, *Phys. Rev. B: Condens. Matter Mater. Phys.*, 2003, **67**, 125110.
25 M. Amsler, *Phys. Rev. B*, 2019, **99**, 060102.
26 P. Tsuppayakorn-aek, P. Phansuke, P. Kaewtubtim, R. Ahuja and T. Bovornratanaraks, *Comput. Mater. Sci.*, 2021, **190**, 110282.
27 J. M. Sanchez, F. Ducastelle and D. Gratias, *Physica A*, 1984, **128**, 334–350.
28 A. van de Walle and G. Ceder, *J. Phase Equilib.*, 2002, **23**, 348–359.
29 A. Van De Walle, M. Asta and G. Ceder, *CALPHAD: Comput. Coupling Phase Diagrams Thermochem.*, 2002, **26**, 539–553.
30 P. Giannozzi, S. Baroni, N. Bonini, M. Calandra, R. Car, C. Cavazzoni, D. Ceresoli, G. L. Chiarotti, M. Cococcioni, I. Dabo, A. D. Corso, S. de Gironcoli, S. Fabris, G. Fratesi, R. Gebauer, U. Gerstmann, C. Gougoussis, A. Kokalj, M. Lazzeri, L. Martin-Samos, N. Marzari, F. Mauri, R. Mazzarello, S. Paolini, A. Pasquarello, L. Paulatto, C. Sbraccia, S. Scandolo, G. Sclauzero, A. P. Seitsonen, A. Smogunov, P. Umari and R. M. Wentzcovitch, *J. Phys.: Condens. Matter*, 2009, **21**, 395502.
31 A. Ektarawong, T. Bovornratanaraks and B. Alling, *Phys. Rev. B*, 2020, **101**, 134104.
32 P. Tsuppayakorn-aek, P. Pluengphon, P. Phansuke, B. Inceesungvorn, W. Busayaporn, P. Kaewtubtim and T. Bovornratanaraks, *Sci. Rep.*, 2021, **11**, 1–7.
33 J. P. Perdew, K. Burke and M. Ernzerhof, *Phys. Rev. Lett.*, 1996, **77**, 3865–3868.
34 S. J. Clark, M. D. Segall, C. J. Pickard, P. J. Hasnip, M. J. Probert, K. Refson and M. Payne, *Z. Kristallogr.*, 2005, **220**, 567–570.
35 A. D. Becke and E. R. Johnson, *J. Chem. Phys.*, 2006, **124**, 221101.
36 G. Kresse and J. Furthmüller, *Phys. Rev. B: Condens. Matter Mater. Phys.*, 1996, **54**, 11169–11186.
37 A. D. Becke and K. E. Edgecombe, *J. Chem. Phys.*, 1990, **92**, 5397–5403.
38 V. L. Deringer, A. L. Tchougréeff and R. Dronskowski, *J. Phys. Chem. A*, 2011, **115**, 5461–5466.
39 S. Maintz, V. L. Deringer, A. L. Tchougréeff and R. Dronskowski, *J. Comput. Chem.*, 2016, **37**, 1030–1035.
40 P. Tsuppayakorn-aek, W. Luo, R. Ahuja and T. Bovornratanaraks, *Sci. Rep.*, 2018, **8**, 3026.
41 P. Tsuppayakorn-aek, W. Luo, T. Watcharatharapong, R. Ahuja and T. Bovornratanaraks, *Sci. Rep.*, 2018, **8**, 5278.
42 P. Tsuppayakorn-aek, W. Luo, W. Pungtrakoon, K. Chuenkingkeaw, T. Kaewmaraya, R. Ahuja and T. Bovornratanaraks, *J. Appl. Phys.*, 2018, **124**, 225901.
43 P. Tsuppayakorn-aek, W. Chaimayo, U. Pinsook and T. Bovornratanaraks, *AIP Adv.*, 2015, **5**, 097202.
44 P. Jimlim, P. Tsuppayakorn-aek, T. Pakornchote, A. Ektarawong, U. Pinsook and T. Bovornratanaraks, *RSC Adv.*, 2019, **9**, 30964–30975.
45 K. Kotmool, P. Tsuppayakorn-aek, T. Kaewmaraya, U. Pinsook, R. Ahuja and T. Bovornratanaraks, *J. Phys. Chem. C*, 2020, **124**, 14804–14810.
46 P. Tsuppayakorn-aek, J. Zhang, W. Luo, Y. Ding, R. Ahuja and T. Bovornratanaraks, *Phys. Status Solidi B*, 2021, **258**, 2000279.
47 M. Di Gennaro, S. K. Saha and M. J. Verstraete, *Phys. Rev. Lett.*, 2013, **111**, 025503.
48 F. Tran and P. Blaha, *Phys. Rev. Lett.*, 2009, **102**, 226401.
49 K. Boulenouar, M. Bouslama, A. Mokadem, S. Vizzini, Z. Lounis, A. Abdellaoui, B. Reguad, M. Bedrouni, K. Hamaida, T. Guenouna and M. Ghaffour, *J. Phys. Chem. C*, 2017, **121**, 8345–8352.
50 F. Tran and P. Blaha, *J. Phys. Chem. A*, 2017, **121**, 3318–3325.
51 T. Bovornratanaraks, R. Ahuja and P. Tsuppayakorn-aek, *Mater. Res. Express*, 2021, **8**(10), 105901.
52 S. Maintz, V. L. Deringer, A. L. Tchougréeff and R. Dronskowski, *J. Comput. Chem.*, 2013, **34**, 2557–2567.
53 Z. Wu, R.-D. Hoffmann, D. Johrendt, B. D. Mosel, H. Eckert and R. Pöttgen, *J. Mater. Chem.*, 2003, **13**, 2561–2565.
54 E. M. Seibel, L. M. Schoop, W. Xie, Q. D. Gibson, J. B. Webb, M. K. Fuccillo, J. W. Krizan and R. J. Cava, *J. Am. Chem. Soc.*, 2015, **137**, 1282–1289.
55 S. Lotfi, A. O. Oliynyk and J. Brgoch, *Inorg. Chem.*, 2018, **57**, 10736–10743.
56 A. A. Adeleke, E. Stavrou, A. O. Adeniyi, B. Wan, H. Gou and Y. Yao, *Phys. Rev. B*, 2020, **102**, 134120.